



Intermetallic ferric nickel silicide alloy derived from magadiite by magnesiothermic reaction as bifunctional electrocatalyst for overall water splitting

Xuyang Jing¹, Yang Mu¹, Zhanming Gao¹, Xueying Dong¹, Changgong Meng^{1,2}, Chi Huang³, and Yifu Zhang¹ (✉)

¹ School of Chemistry, Dalian University of Technology, Dalian 116024, China

² College of Environmental and Chemical Engineering, Dalian University, Dalian 116622, China

³ College of Chemistry and Molecular Sciences, Wuhan University, Wuhan 430072, China

Received: 15 July 2023 / Revised: 7 October 2023 / Accepted: 9 October 2023

ABSTRACT

As the cleanest energy source, hydrogen energy is regarded as the most promising fuel. Water electrolysis, as the primary means of hydrogen production, has constantly been the focus of attention in the energy conversion field. Developing eco-friendly, cheap, safe and efficient catalysts for electrochemical water splitting (EWS) is the key challenge. Herein, the intermetallic silicide alloy is first synthesized via a facile magnesiothermic reduction and employed as bifunctional electrocatalysts for EWS. Ferric-nickel silicide (denoted as FeNiSi) alloy is designed and shows a good electrocatalytic performance for EWS. The lattice distortions of FeNiSi enhance the electrocatalytic activity. Besides, the porous structure affords more active sites and improves the reaction kinetics. As a consequence, FeNiSi delivers an excellent performance with overpotential of 308 mV for oxygen evolution reaction (OER) and 386 mV for hydrogen evolution reaction (HER) at 10 mA·cm⁻² in 1 M KOH. The stability structure of intermetallic silicide achieves an outstanding durability with an unchanged potential of 1.66 V for overall water splitting at 10 mA·cm⁻² for 15 h. This work not only provides a facile method for the synthesis of intermetallic silicide with considerable porous structures, but also develops the potential of intermetallic silicide alloy as bifunctional electrocatalysts for EWS, which opens up a new avenue for the design and application of intermetallic silicide alloy.

KEYWORDS

bimetallic silicide, magadiite, magnesiothermic reduction, bifunctional electrocatalyst, overall water splitting

1 Introduction

In reaction to the increasingly severe environmental problems and energy crisis, the development of low-cost clean energy has become an important scientific research topic [1–6]. The European Patent Office (EPO) and the International Renewable Energy Agency (IRENA) jointly declared “Patent Insight Report: Innovation Trends in Electrolysers for Hydrogen Production” in 2022, which investigated the global evolution of published patent applications in the field of electrolytic cells used for hydrogen production by hydroelectrolysis from 2005 to 2020, and revealed the trend and vitality of electrolytic cell technology. As the most representative clean energy, hydrogen energy has the characteristics of huge potential reserves, high calorific value, light weight and environmental protection [7–9]. It can effectively deal with climate change, curb the process of global warming, vigorously promote the aim of “carbon peaking and carbon neutrality”, and realize the energy transformation of society [10–12]. Against this background, water electrolysis as one of the

most important means of hydrogen production has been widely and deeply studied. Electrolytic water has the advantages of cheap, easy and environmental protection, and its production only depends on the renewable resources: water and electricity [13–15]. However, what really limits the development and practical application of electrolytic water technology is electrocatalytic materials. At present, common catalysts, such as precious metals [16–18], carbides [19], nitrides [20], and sulfides [21–23], are mostly single-function catalysts, which limits the practical application of water electrolysis for hydrogen production [24]. Therefore, the research and development of efficient, stable, cheap and environmentally friendly bifunctional electrocatalytic materials will become the main research direction in the field of electrocatalysis in the future [14, 25].

Transition metal silicide alloy is an important refractory intermetallic compound with outstanding heat, chemical and mechanical stability. The metal atoms in the structure are separated by silicon atoms, thus improving the utilization of metal atoms, and the high stability and heat resistance prevent the

© The Author(s) 2024. Published by Tsinghua University Press. The articles published in this open access journal are distributed under the terms of the Creative Commons Attribution 4.0 International License (<http://creativecommons.org/licenses/by/4.0/>), which permits use, distribution and reproduction in any medium, provided the original work is properly cited.

Address correspondence to Yifu Zhang, yfzhang@dlut.edu.cn

agglomeration of metal atoms during use. On the one hand, considering silicon is in the same group as carbon in the periodic table of elements, transition metal silicide has similar physical and chemical properties to carbide, so it is widely used in energy-related fields [26–30]. For instance, Kumar and his coworker synthesized a nickel silicide via a liquid-phase synthesis in molten salts, and it delivered an overpotential of 570 mV at 10 mA·cm⁻² for oxygen evolution reaction (OER) [31]. Hausmann and his coworker prepared phase-pure FeSi from mixture of elemental iron and silicon by arc-melting with an overpotential of 369 mV at 500 mA·cm⁻² for OER [32]. Chang et al. prepared NiSi nanowires by using a chemical vapor deposition associated with an electrochemical tuning, and the products were used for electrocatalyst with low overpotentials of 296 and 156 mV for the OER and hydrogen evolution reaction (HER) [33]. Previous results indicate that there is still a great room for the improvement of the electrocatalytic property of transition metal silicide. On the other hand, so far, the commonly used methods for preparation of silicide are chemical vapor deposition [26, 34], molten salt [35, 36], vapor–liquid–solid method [37], the sol–gel technique [38], and so on. These preparation methods are always associated with high temperatures, high vacuum or employment of expensive and unstable raw materials [37–39]. Therefore, a cheap, safe, and environmentally friendly method for the synthesis of silicide is of great significance for its sustainable development and worth to be explored. Nickel silicide has been concerned and deeply studied for its low resistance and high metal activity, especially its application in electrochemical field [28, 40]. In addition, many recent studies have shown that Fe–Ni based materials have considerable potential in the field of electrochemical water splitting (EWS) [40–42]. The aim of this work is to develop a low-cost environmentally friendly route for the preparation of iron nickel silicide as the bifunction electrolytic water catalyst.

In the present work, high performance bifunctional electrocatalyst intermetallic silicide ferric-nickel silicide (denoted as FeNiSi) alloy is first time synthesized through metallothermic reduction by using metallic silicate, which is prepared by a one-pot hydrothermal reaction of natural clay magadiite. The as-prepared metallic silicide possesses uniform morphological considerable pore structures, which allows FeNiSi to expose more active sites and more optimized reaction kinetics. Besides, the Fe–Ni synergies and heterostructures can enhance the activity by changing the electronic structure of FeNiSi. Consequently, FeNiSi possesses an outstanding bifunctional electrocatalyst for overall water splitting. The electrochemical performance of FeNiSi delivers an overpotential of 368 mV for HER and 309 mV for OER at 10 mV·cm⁻² in 1 M KOH. The mild and convenient synthesis method, appreciable porous structure and excellent bifunctional catalytic performance will provide a new idea for the preparation of silicide applied to the energy storage and conversion.

2 Experimental section

2.1 Pretreatment of precursors (metallic silicates)

All chemicals were of analytical grade and utilized without any purification. The original magadiite (mag) was prepared by the hydrothermal method based on the works with some improvement [43, 44], as represented in the Electronic Supplementary Material (ESM). The bimetallic silicate Fe_xNi_{2-x}SiO₄ was prepared by a hydrothermal process. 0.06 g mag was added to 10 mL deionized water by ultrasonication named

Solution One. 207 mg FeCl₃ and 207 mg NiCl₂ were added to 25 mL deionized water named Solution Two. Then Solution One and Solution Two are blended and stirred. After 15 min, 534.6 mg NH₄Cl and 4 mL NH₃ H₂O are added and stirred for 45 min. The mixture was removed to a 50 mL Teflon-lined stainless-steel autoclave and kept at 180 °C for 24 h. The samples were collected by washing with deionized water and ethanol, and dried at 65 °C in vacuum for 12 h. Similarly, single metal silicates Fe₂SiO₄ and Ni₂Si₂O₅(OH)₄ were prepared to compare by the same method control the amount of metal as bimetallic silicate Fe_xNi_{2-x}SiO₄, respectively.

2.2 Synthesis of intermetallic silicide alloy (MSi, M = Fe, Ni, or mixture)

The bimetallic silicide alloy (denoted as FeNiSi) was prepared by a magnesiothermic reduction. 0.06 g bimetallic silicate, 0.06 g magnesium powder and 0.18 g NaCl were mixed in an agate mortar and grind slowly to mix well. Then, the mixture was transferred to a graphite boat and calcined in a tube furnace in an Ar atmosphere at 650 °C for 8 h to obtain FeNiSi. The annealed power was then treated by 1 M HCl solution and 5% HF to remove the MgO and residual SiO₂. Subsequently, the products were washed with deionized water and ethanol several times and dried at 60 °C for 12 h. The monometallic silicides (ferric silicide denoted as FeSi, and nickel silicide denoted as NiSi) were synthesised through the same method by using Fe₂SiO₄ and Ni₂Si₂O₅(OH)₄ as raw materials.

2.3 Characterizations

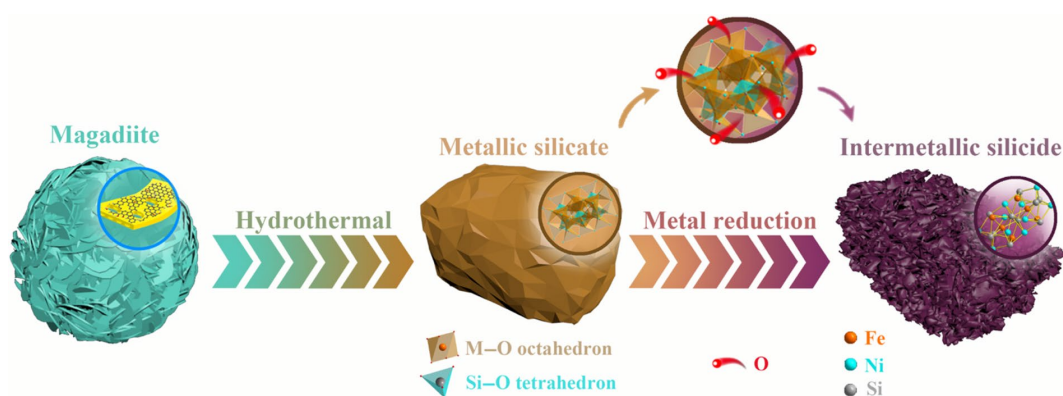
The composition, morphology and structure were tested by field emission scanning electron microscopy (FE-SEM), transmission electron microscopy (TEM), nitrogen adsorption/desorption isotherms, X-ray powder diffraction (XRD), X-ray photoelectron spectroscopy (XPS), and Fourier-transform infrared spectra (FT-IR).

The preparation of electrodes and their electrochemical characterizations were studied by cyclic voltammetry (CV), linear sweep voltammetry (LSV) and electrochemical impedance spectroscopy (EIS). All above details were represented in the ESM.

3 Results and discussion

3.1 Characterization of intermetallic silicide alloy

Scheme 1 briefly sketches the contour of the preparation of FeNiSi. The synthesis of FeNiSi mainly consists of two parts: (1) the original mag is converted to metallic silicate (precursor) through a hydrothermal process; (2) the precursor is mixed with NaCl and Mg reductants, and annealed at 650 °C under Ar atmosphere. Mag, a kind of lamellar silicate which occurs widely in nature, is used here as a silicon source. In the hydrothermal process, owing to the alkaline environment, the lamellar slowly dissolve to release silicate ions and they react with the metal cations to form homogeneous and well-defined metallic silicates. Then, the as-prepared metallic silicates, Mg powder and NaCl were mixed evenly by grinding, and the mixture was transferred into the graphite boat to heat treatment. Mg, as a reducing agent, is usually thought to be activated at around 550 degrees and adhered to the surface of silicate [45]. Subsequently, Si of silicon-oxygen tetrahedron and relatively inert metals (iron, nickel) of metallic silicate are reduced by activated Mg, and the process



Scheme 1 The synthesis of intermetallic ferric nickel silicide alloy.

releases intense heat. The exothermic heat will be absorbed by the silicate and NaCl. Although the reaction temperature is not high enough for Mg and silicate to melt, the heat released by the surface reaction causes the mixture to slowly melt into the silicate and allow the reaction to proceed further. The MgO generated by the reaction and the NaCl that melts into the product will be dissolved and removed after washing. This process will leave many pore structures in the prepared metallic silicide alloy, so that the prepared silicide has a high specific surface area, which has a very positive effect on its electrocatalytic performance. It is worth mentioning that the magnesium thermal reaction is often used to produce pure silicon from silicon dioxide. Here, for the first time, metallic silicide alloys are prepared via a one-step magnesiothermic reduction by using metallic silicates as raw material.

The crystal structure and morphology of precursors are conformed by XRD and FE-SEM. The results of XRD patterns (Fig. S1 in the ESM) proved that the precursors are typical metallic silicates. Two monometallic silicates respectively correspond to the standard XRD cards of Fe_2SiO_4 (JCPDS, No. 74-1002) and $\text{Ni}_3\text{Si}_2\text{O}_5(\text{OH})_4$ (JCPDS, No. 22-754), respectively. The bimetallic silicate has all diffraction peaks of both Fe_2SiO_4 and $\text{Ni}_3\text{Si}_2\text{O}_5(\text{OH})_4$. The XRD patterns of these three silicates are free of impure peaks, which demonstrate the pure and well-defined metallic silicates. The morphology of precursors is characterized by FE-SEM (Fig. S2 in the ESM), the iron-containing silicates have a blocky morphology with smooth surface. Unlike the two above, $\text{Ni}_3\text{Si}_2\text{O}_5(\text{OH})_4$ presents a rough block composed of nanoparticles. Although the three morphologies are different, their morphologies are very uniform. Combined with the conclusion of XRD patterns, precursors are all pure phase metallic silicates. Compared with the poly-phase metal silicide prepared by melting and solid phase reaction, the homogeneous precursor will make the metal ions and silicon atoms evenly distributed according to the stoichiometry ratio, and finally get the metal silicide alloys with more uniform structure. The FE-SEM images and element mapping (Fig. 1 and Fig. S3 in the ESM) of FeNiSi, FeSi and NiSi further provide direct evidence for homogeneous and porous structure. FeSi (Fig. 1(a)) composed of nanoparticles around 100 nm in size, and a local magnification FE-SEM image (Fig. 1(d)) shows that gaps between the nanoparticles indicates the material with porous structure. The morphology of NiSi (Figs. 1(b) and 1(e)) is similar to that of FeSi, except the smaller nanoparticles, which result in a denser structure and potentially smaller pore size. Unlike FeSi and NiSi, FeNiSi is more like a skeleton of dried sponges (Figs. 1(c) and 1(f)). The hollow skeleton creates a well-developed porous structure. It is worth mentioning

that the unique three-dimensional (3D) framework structure can expose more active sites, which can increase the possibility for further *in-situ* OER and HER reactions. All three metallic silicide alloys are homogenous with optimal porous structure. The element mapping (Fig. 1(g)) shows compositional homogeneity of the as-prepared silicide. The results show FeNiSi contains Fe, Ni and Si, and homogeneously distributed. Similar conclusions are also obtained from FeSi and NiSi (Fig. S3 in the ESM). These results indicate that the metallic silicide alloy with porous can be obtained through the magnesiothermic reduction method by using metallic silicates as precursor.

In order to further analyze the details of the morphology and structure, TEM measurements are carried out for intermetallic silicide. From the TEM image of FeSi (Fig. 2(a)), the FeSi nanoparticles are composed of many 10 nm wide nanostrips. Among the nanoparticles made up of many nanostrips, there are many obvious light-colored blocks, representing a large number of porous in the structure. In the high-resolution TEM image (Fig. 2(d)), a series faint lattice fringes with a spacing of 0.25 nm can be seen, corresponding to (002) crystal plane. The interior of the NiSi shows many mottled shades of color, representing a stack of nanoparticles (Fig. 2(b)). Compared with FeSi, the overall structure is more compact, and the porous are more dispersed and smaller. This is consistent with the conclusion obtained by FE-SEM. The high resolution TEM image (Fig. 2(e)) reveals a crystalline structure of NiSi with distinct lattice spacing of 0.2 nm which is corresponding of (111) crystallographic plane. The TEM image of FeNiSi (Fig. 2(c)) reveals that the internal lamellar structure is interwoven, and the lamellar thickness is about 3 nm, which is in good agreement with the result of FE-SEM. Significantly, differed from FeSi and NiSi, FeNiSi also has clear lattice stripes, but they are not arranged neatly. The uniform distribution of Fe and Ni atoms causes distortions in the lattice, as shown in Fig. 2(f). The lattice distortions of FeNiSi fluctuated between 0.2–0.25 nm, which directly leads to the distortion of the lattice. The lattice distance tends to cause abundance crystal defects, which can enhance the electrocatalytic activity of active sites [46, 47]. These images described the morphology and confirm the pore structure of metallic silicide alloys. Although the pore structure is not directly related to the activity of the electrocatalyst, the abundant porous can expose more metal active sites and promote the occurrence of surface catalytic reactions [48].

All morphologies indicate that the intermetallic silicides have porous structure. The pore structure parameters are determined by the nitrogen adsorption/desorption isotherms. The adsorption/desorption isotherms of FeSi, NiSi, and FeNiSi (Fig.

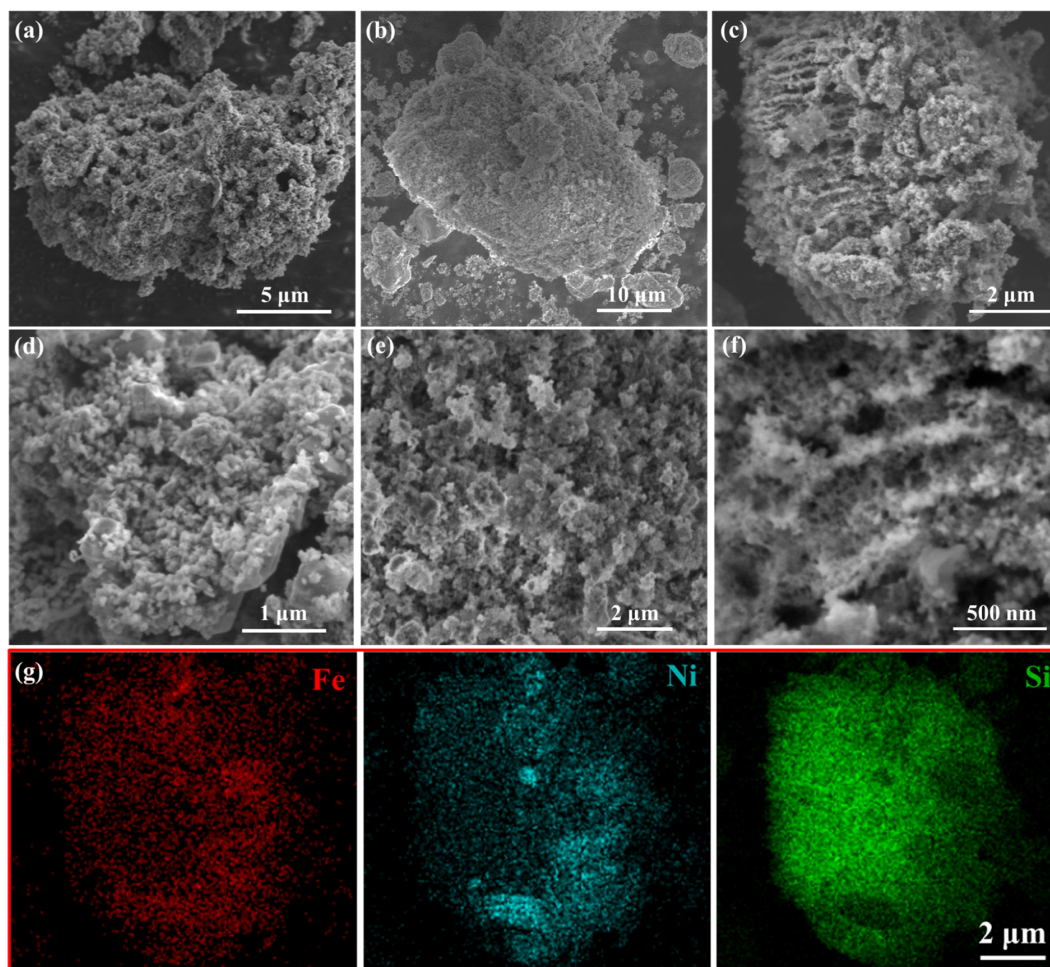


Figure 1 FE-SEM images of intermetallic silicide alloy: ((a) and (d)) FeSi; ((b) and (e)) NiSi; and ((c) and (f)) FeNiSi. (g) Mapping images of FeNiSi.

3(a) exhibit representative type-IV isotherm (IUPAC classification), which suggest the mesoporous structure. The Brunauer–Emmett–Teller (BET) surface area of FeSi, NiSi, and FeNiSi are calculated to be 139, 82, and 118 $\text{m}^2\cdot\text{g}^{-1}$, respectively. What is worth mentioning, although the specific surface area of FeSi is slightly larger than FeNiSi, the subsequent pore size distribution (Fig. 3(b)) shows that FeNiSi has more mesoporous structures which are beneficial for the mass transfer and oxygen diffusion [48, 49]. All above results indicate that the as-synthesised intermetallic silicide alloys possess considerable specific surface area and rich pore structure. The crystal structure of these intermetallic silicide is confirmed by XRD patterns (Fig. 3(c)). After magnesiothermic reduction process, all the characteristic diffraction peaks of intermediate silicates disappear, which proves that silicates have been completely reduced. The XRD patterns of NiSi well match with the standard XRD cards of Ni_3Si (JCPDS, No. 65-143) without heterodox peaks. The XRD pattern of FeSi has only a weak crest, indicating its amorphous structure. The results show that although various metal silicides can be prepared by magnesiothermic reaction, their structures are different. The XRD pattern of FeNiSi has the diffraction peaks of both Fe_2Si (JCPDS, No. 83-1259) and Ni_3Si (JCPDS, No. 65-143) without impure peaks, which proves the successful preparation of intermetallic silicide alloy. Besides, the diffraction peaks of FeNiSi are weak, which are attributed to the lattice distance [50, 51]. To further confirm the structural information bonds between atoms of intermetallic silicide, the FT-IR spectra are tested for precursor and metallic silicide alloys. By comparing the FT-IR spectra of

precursor and FeNiSi (Fig. S5(a) in the ESM), it is easy to observe the absence of peak at about 1000 cm^{-1} , which corresponding to Si–O bond. This means that the original Si–O tetrahedron no longer exists. The FT-IR of other samples (Fig. S5(b) in the ESM) also showed a similar phenomenon, and only a small amount of Si–O bonds remained in NiSi [52].

The surface electronic structure information of the product was collected by XPS spectra. The XPS survey spectra (Fig. S4 in the ESM) of FeSi, NiSi, and FeNiSi demonstrate the existence of Si and the corresponding metallic elements, respectively. The embedded graph is a local magnification of Fe and Ni, further clear proof of metal elements in each sample. The Fe 2p spectra (Fig. 3(d)) of FeSi and FeNiSi show a similar electronic structure. The peaks related to Fe $2p_{1/2}$ are located in 725.15 and 725.28 eV for FeSi and FeNiSi, respectively. The peaks assigned to Fe $2p_{3/2}$ are situated at 711.08 and 711.56 eV for FeSi and FeNiSi, respectively. The peaks at 725.14 and 725.28 eV are related to Fe $2p_{1/2}$ for FeSi and FeNiSi, respectively. The peaks around 714.05 and 737.37 eV for FeSi and 715.39 and 736.21 eV for FeNiSi are corresponding to the characteristic satellites' peaks (labelled Sat.). The separations of Fe $2p_{3/2}$ and Fe $2p_{1/2}$ for FeSi and FeNiSi are about 14 eV, which demonstrates the iron is in a trivalent state [53, 54]. The peak fitting results of Ni 2p spectra (Fig. 3(e)) of NiSi and FeNiSi show that the peaks at 873.75 and 873.85 eV for Ni $2p_{1/2}$ of NiSi and FeNiSi, respectively. The peaks at 856.13 and 856.20 eV for Ni $2p_{3/2}$ of NiSi and FeNiSi, respectively. The spin-orbit splitting values of Ni $2p_{1/2}$ and Ni $2p_{3/2}$ are calculated to be 17.6 eV. The peaks at 862.00 and 880.00 eV for NiSi, 861.99 and

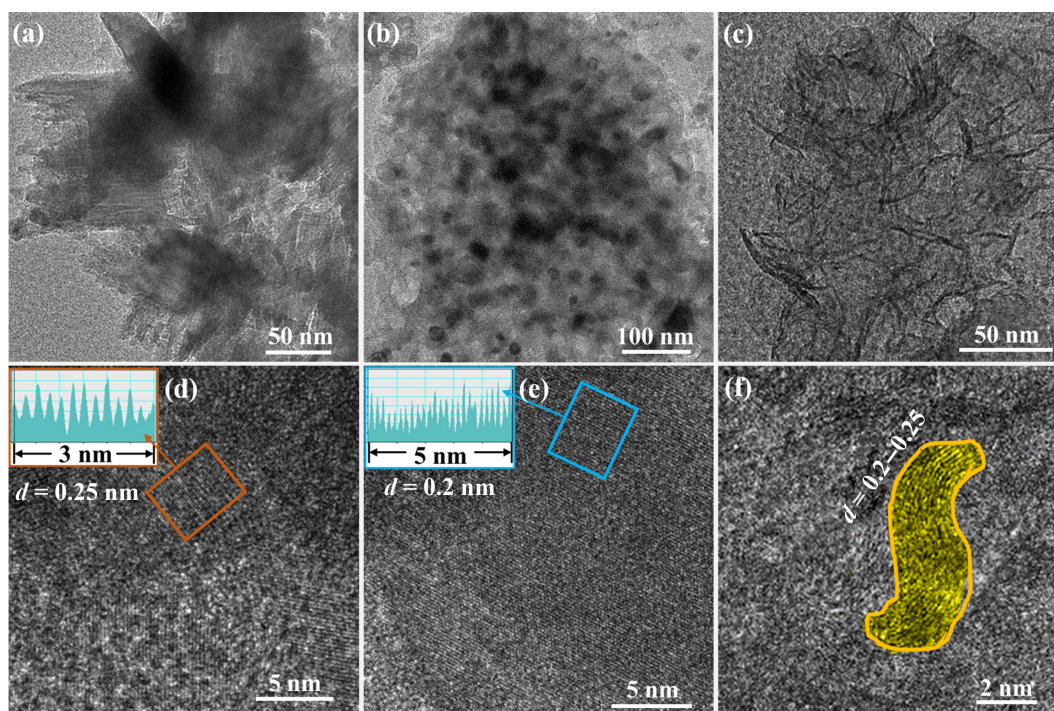


Figure 2 TEM images of intermetallic silicide: ((a) and (d)) FeSi; ((b) and (e)) NiSi; and ((c) and (f)) FeNiSi.

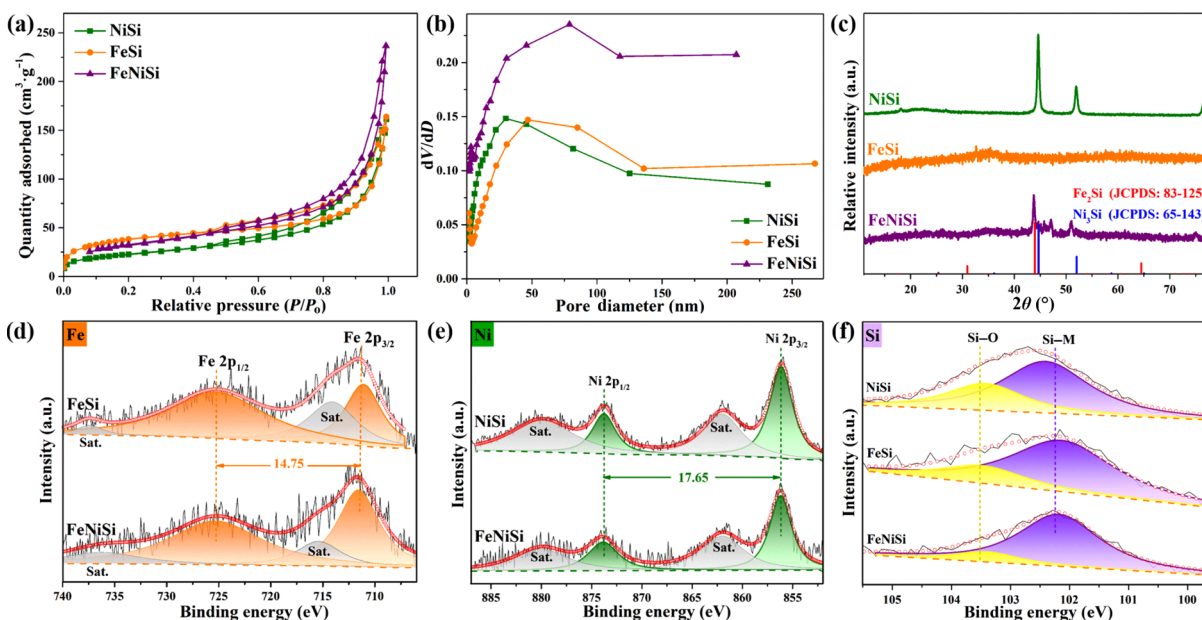


Figure 3 Characterizations of intermetallic silicide: (a) nitrogen adsorption/desorption isotherms; (b) pore-size distribution calculated by the Barrett–Joyner–Halenda (BJH) method; and (c) XRD patterns. (d)–(f) XPS spectra: (d) Fe 2p, (e) Ni 2p, and (f) Si 2p.

880.02 eV for FeNiSi are ascribed to Sat. The binding energy of Ni 2p spectrum and Fe 2p spectrum are slightly higher than metallic Fe and Ni, which means the low electron density and stronger interaction of metallic sites with HO*, O*, and OOH* [40, 55]. In the Si 2p region (Fig. 3(f)), the peak at 103.42 eV can be assigned to surface Si–O species, which probably arises from exposure to air during preparation and storage. The peaks of M–Si (M = Fe or Ni) are located at 101.77, 102.41, and 102.18 eV for FeSi, NiSi, and FeNiSi, respectively. The reason for this phenomenon (the bonding energy of M–Si follows the order NiSi > FeNiSi > FeSi) is the electronegativities (χ) of Ni ($\chi_{\text{Ni}} = 1.91$), Fe ($\chi_{\text{Fe}} = 1.83$), and Si ($\chi_{\text{Si}} = 1.90$) [56]. The difference in the binding energy of FeSi, NiSi, and FeNiSi directly proves the synergy in FeNiSi, and the material

is thus activated. Both of peaks position and orbital separation energy prove that the Ni in NiSi and FeNiSi are bivalent. The above results not only explain the electronic structure of the sample surface and the valence state of the metal elements, but also prove that the state of the metal ion is the same whether it is in monometallic silicide or in bimetallic silicide.

3.2 HER performance of intermetallic silicide alloy

The electrocatalytic performance was evaluated using a standard three-electrode system in 1 M KOH electrolyte. The HER performances of intermetallic silicide are first investigated by LSV at 5 mV·s⁻¹ (Fig. 4(a)). Among the three kinds of as-prepared silicides, with the potential decrease, FeNiSi has the most drastic

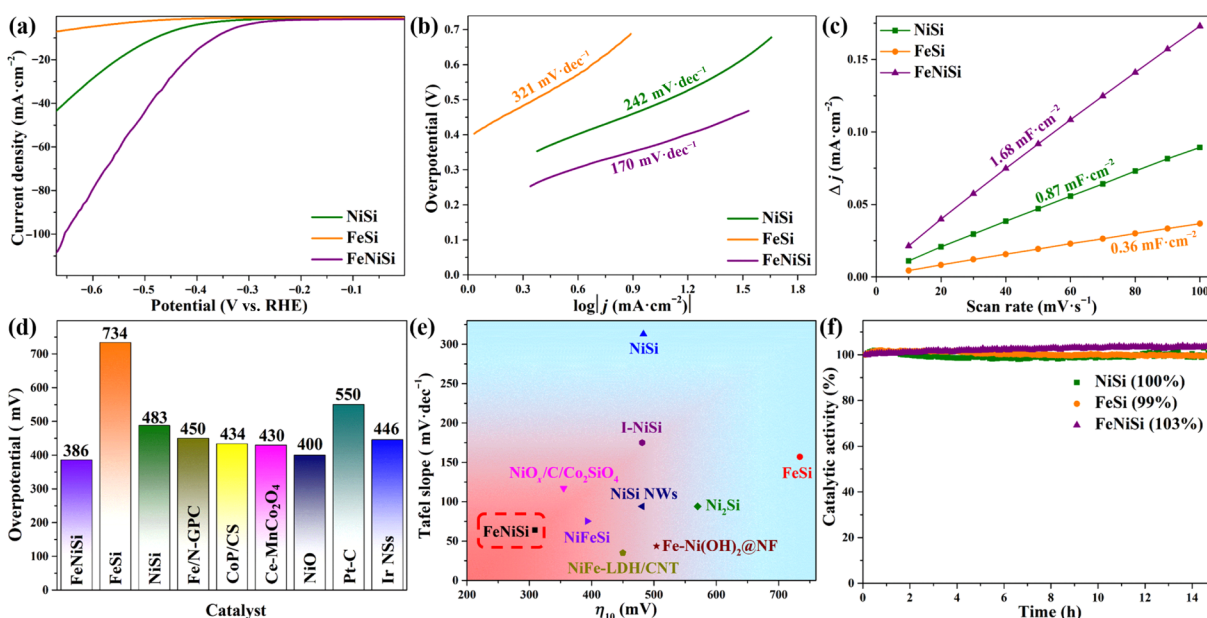


Figure 4 (a) HER polarization curves of intermetallic silicide at $5 \text{ mV}\cdot\text{s}^{-1}$. (b) The corresponding Tafel plots from (a). (c) Scan rate vs. current density diagram of intermetallic silicide. (d) Comparing analysis of HER overpotential at $10 \text{ mA}\cdot\text{cm}^{-2}$. (e) Overpotential and Tafel slope comparison with other transition metal electrocatalysts. (f) Chronopotentiometry experiments of intermetallic silicide for HER.

change in response current, indicating that FeNiSi achieves the lowest overpotential. All intermetallic silicide alloys deliver a HER activity in alkaline electrolyte. At $10 \text{ mA}\cdot\text{cm}^{-2}$, the overpotential of FeSi, NiSi, and FeNiSi are measured to be 734, 483, and 386 mV, respectively. The lower overpotential of FeNiSi indicates that the lattice defects and synergistic effects reinforce the electrocatalytic activity.

Another important factor, Tafel plots (Fig. 4(b)), which are always used to reflect the reaction kinetics and rate-determining steps during the electrocatalytic process, are calculated based on the polarization curves. The approximate Tafel slopes indicate the same reaction pathway and rate-determining steps of FeSi, NiSi, and FeNiSi. In alkaline electrolyte, when the Tafel slope is larger than $120 \text{ mV}\cdot\text{dec}^{-1}$, Volmer process ($\text{H}_2\text{O} + \text{e}^- \leftrightarrow \text{H}_{\text{ads}} + \text{OH}^-$) is generally considered to be the rate-limiting step [14, 57]. Among three metallic silicide alloys, FeNiSi deliver the lowest Tafel slope ($170 \text{ mV}\cdot\text{dec}^{-1}$), indicating the faster hydrogen evolution rate than FeSi and NiSi. The main reason is that a large number of mesoporous structures can promote the infiltration of catalyst–electrolyte interface. And the sponge-like morphology allows FeNiSi to expose more active sites, which can greatly increase the probability of electrochemical surface reaction. The CV curves at different scan rate within non-Faraday region (Fig. S6 in the ESM) are measured to calculate the double layer capacitances (C_{dl}), which are related to electrochemical active surface areas (ECSA). The C_{dl} of FeSi, NiSi, and FeNiSi for HER (Fig. 4(c)) are calculated to be 0.36, 0.87, and $1.68 \text{ mF}\cdot\text{cm}^{-2}$. FeNiSi shows the largest C_{dl} presenting the largest ECSA, which means the most active sites exposed. In order to reflect this conclusion more intuitively, we normalized LSV curve by C_{dl} (Fig. S7(a) in the ESM) and BET specific surface area (Fig. S7(b) in the ESM). The results show that after the normalization by C_{dl} and specific surface area, the advantage of the electrocatalytic performance of FeNiSi is more prominent. These result more intuitively indicates that FeNiSi possess the highest reactivity and the most active sites per unit surface. The comparison between as-prepared silicide alloys and transition metal HER electrocatalysts reported these years (Fig. 4(d) and Table S1 in the ESM) shows that FeNiSi has

an ideal hydrogen evolution overpotential. Besides, the overpotential vs. Tafel slope plot (Fig. 4(e)) more comprehensively reflects FeNiSi's superiority for HER. The EIS spectra for HER (Fig. S8 in the ESM) show that three kinds of metal silicides deliver a small semicircle in the high frequency region, indicating rapid charge transfer. The steep curve in the high frequency region indicates the rapid ion migration rate at the electrode–electrolyte interface, which may due to the porous structure. Similar curves indicate similar dynamic processes of the three during the HER process. Among them, FeNiSi showed the best electrocatalytic performance under similar kinetic conditions. This phenomenal can further demonstrate that the excellent performance of FeNiSi is based on the activity of its nature. Chronopotentiometry experiments of FeSi, NiSi, and FeNiSi for HER at $10 \text{ mA}\cdot\text{cm}^{-2}$ indicate the overpotential can be maintained stably for at least 15 h without significant changes (Fig. 4(f)). On the one hand, the outstanding HER stability is attributed to the structural stability of the metal silicide alloy. On the other hand, the rich pore structure can alleviate the structural stress and accelerate the escape of bubbles.

3.3 OER performance of intermetallic silicide alloy

The standard three-electrode system is also applied to evaluate OER electrocatalytic performance. The OER process in alkaline electrolyte is always considered to be a multi-electron transfer process, and therefore is considered to be a rate-controlled step for overall water splitting. Figure 5(a) shows the LSV curves of FeSi, NiSi, and FeNiSi for OER at $5 \text{ mV}\cdot\text{s}^{-1}$, and the overpotential at $10 \text{ mA}\cdot\text{cm}^{-2}$ are measured to be 802, 488, and 309 mV, respectively. Obviously, the OER activity of FeNiSi is superior to FeSi and NiSi. The huge performance difference between FeNiSi and the others probably originated from the synergistic effect of bimetal and the defects formed by lattice distortion. The corresponding Tafel slope (Fig. 5(b)) presents a similar result from overpotential, and the values are calculated to be 313, 157, and $64 \text{ mV}\cdot\text{dec}^{-1}$ for NiSi, FeSi, and FeNiSi, respectively. Small Tafel slope means that a slight rise of potential will bring about a notable change of current density. The Tafel slope of NiSi and FeSi are

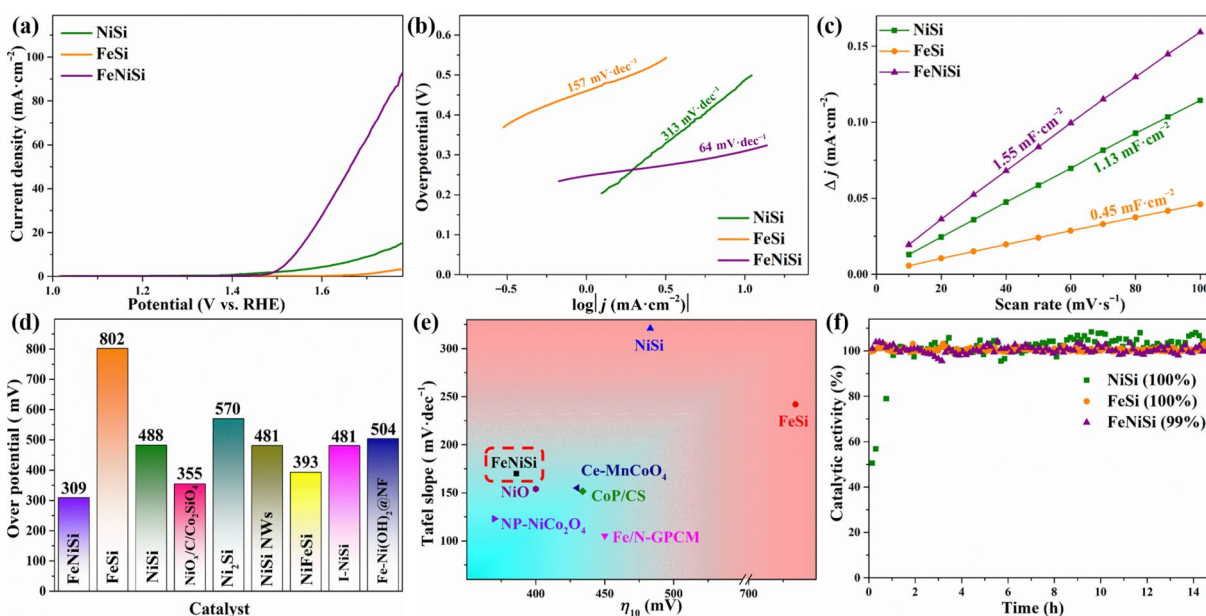


Figure 5 (a) OER polarization curves of intermetallic silicide at 5 mV·s⁻¹. (b) The corresponding Tafel plots from (a). (c) Linear fitting plots used for estimating ECSA of intermetallic silicide. (d) Comparing analysis of the OER overpotential at 10 mA·cm⁻². (e) Overpotential and Tafel slope comparison with other transition metal electrocatalysts. (f) Chronopotentiometry experiments of intermetallic silicide for OER.

larger than 120 mV·dec⁻¹, indicating its rate-determining step is the second elementary reaction ($\text{OH}^- \leftrightarrow \text{OH}_{\text{abs}} + e^-$). However, the Tafel slope of FeNiSi is closer to 60 mV·dec⁻¹, which indicates that first elementary reaction ($\text{OH}_{\text{abs}} + \text{OH}^- \leftrightarrow \text{O}_{\text{abs}} + \text{H}_2\text{O} + e^-$) is the rate-determining step. It can be seen that the OER reactions of FeSi and NiSi are limited by the formation of surface adsorbed hydroxyl radicals (OH_{abs}). But, the rate-determining step of OER reaction of FeNiSi is the formation of surface oxygen free radicals (O_{abs}). The reason for this transformation is the large number of active sites on the surface of FeNiSi, which greatly facilitates the formation of OH_{abs} so that it is no longer the rate-determining step of OER reaction [58]. The C_{dl} of as-synthesized silicide (Fig. 5(c)), which is obtained by a series of CV curves at different scan rates in non-Faraday potential range (Fig. 4(e) and Fig. S9 in the ESM), delivers a value of 0.45, 1.13, and 1.55 mF·cm⁻² for FeSi, NiSi, and FeNiSi, respectively. A corollary of LSV curves normalized by C_{dl} (Fig. S10(a) in the ESM), BET specific surface area (Fig. S10(b)), FeNiSi has the largest ECSA and the most active sites per unit area. The OER overpotential of FeNiSi is lower than that of metallic silicide materials published in recent year for its generous activity sites and outstanding reaction kinetics (Fig. 5(d) and Table S2 in the ESM). The comparison of the overpotential and Tafel slope of as-prepared metallic silicide with recently reported OER materials also shows its superiority (Fig. 5(e)). To further confirm this conclusion, the EIS spectra for OER are tested (Fig. S11 in the ESM). In the high frequency region, the small circle radius of FeNiSi and NiSi is significantly smaller than that of FeSi, which indicates that FeNiSi and NiSi possess a faster charge transfer rate, and the unsatisfactory OER performance of FeSi may be directly related to this. In the low frequency region, FeNiSi has the highest slope, indicating that it has the best ion diffusion ability among the three. The rapid diffusion of ions may be due to the large number of pore structures in the frame structure formed by the internal nanosheets, which may very beneficial for OER process. Electrocatalytic stability is characterized by chronopotentiometry experiments for OER at 10 mA·cm⁻² (Fig. 5(f)), and the result shows that the overpotential of as-prepared metallic silicide remains almost unchanged after 15 h, which

indicates the metallic silicide synthesized by metallothermic reduction can maintain stable structure and catalytic activity during the continuous electrocatalytic reactions. From the OER test above, the lattice imperfection and superior specific surface area make FeNiSi an excellent OER electrocatalytic material.

3.4 Overall water splitting performance of intermetallic silicide alloy

Considering the as-prepared intermetallic silicide delivers both HER and OER electrocatalytic activity, the overall water splitting performance is measured by fabricating the silicide into an electrolyzer. The combination of corresponding LSV of as-prepared metallic silicides without iR compensation is shown in Fig. 6(a), and the potential ranges for current density between ± 10 mA·cm⁻² are marked. In the initial stage of water electrolysis, the system undergoes a thermodynamic process. With the potential rise up, the influence of dynamic factors gradually appears. Therefore, the current density is kept very low in the low voltage region. As the voltage rises further, the current density increases abruptly. The LSV of as-fabricated electrolyzers (Fig. 6(b)) show a potential of 1.66 V to deliver 10 mA·cm⁻² for FeNiSi||FeNiSi, which is very close to noble metal catalyst IrO₂||Pt/C of 1.66 V [59]. The water splitting voltage of FeSi||FeSi (1.74 V) and NiSi||NiSi (1.71 V) are apparently higher than FeNiSi||FeNiSi, in line with the OER and HER properties.

The reasons for the superior performance are further analyzed by EIS spectra (Fig. 6(c)). The semicircle radius of the high frequency region is a good indication that FeNiSi has the smallest charge transfer resistance, while FeSi is the least conductive. The slope of the line in the low frequency region is usually related to ion migration in electrochemical reactions. The steep slopes of the three silicide curves in the low frequency region indicate that the pore structure of them leads to a good ion transport dynamic. Durability of FeNiSi||FeNiSi is performed by chronoamperometric (Fig. 6(d)), and the result shows that the potential remains around 1.65 V after 15 h during the continuous testing with the current density fixed at 10 mA·cm⁻². The excellent stability is closely

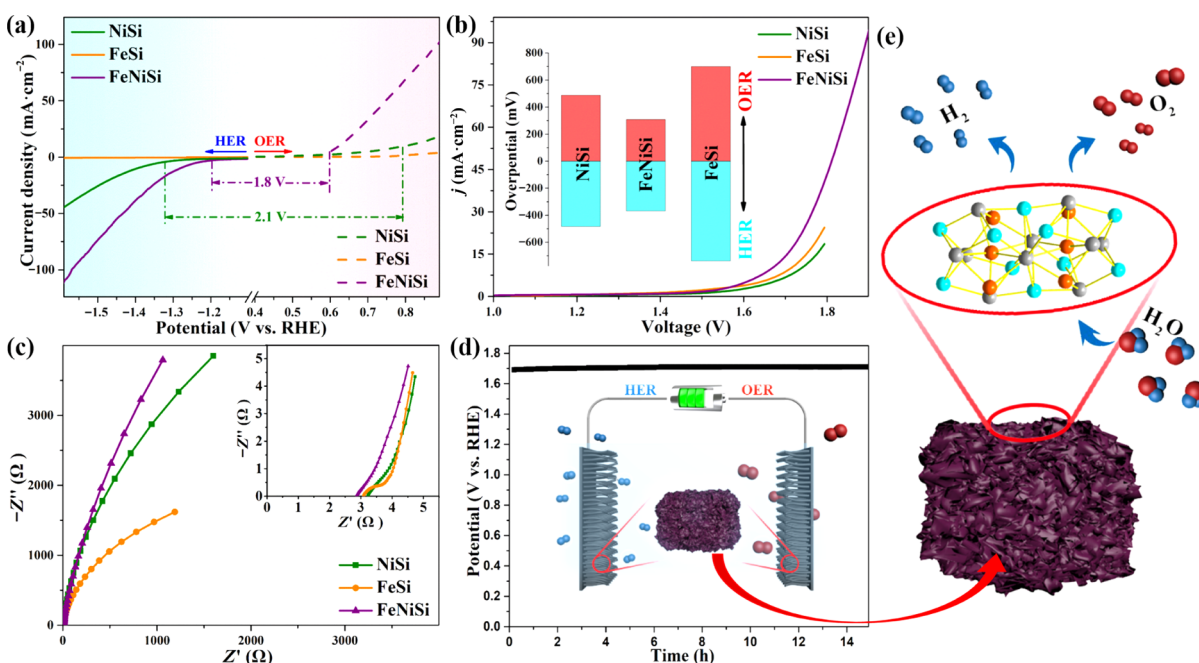


Figure 6 The water splitting performance: (a) the corresponding LSV results of FeSi, NiSi, and FeNiSi without iR compensation; (b) the LSV curves of FeSi||FeSi, NiSi||NiSi, and FeNiSi||FeNiSi for overall water splitting; (c) EIS spectra; (d) chronoamperometric test of the FeNiSi||FeNiSi at 10 mA·cm⁻² for 15 h; and (e) schematic illustration of silicide simultaneously undergoing HER and OER processes.

related to the stable structure of intermetallic silicide. Besides, the porous structure can also improve stability by accelerating the bubble overflow. To explore the stability limit of FeNiSi, an ultra-long stability test is carried out (Fig. S12 in the ESM), and the result shows that the overpotential only increased 60 mV after 120 h of full water splitting. In order to further explore the reasons for the good stability of metal silicide, taking FeNiSi as an example, SEM and TEM images (Fig. S13 in the ESM) were taken after the chronoamperometric. After continuous water electrolysis for 15 h, the morphology of FeNiSi did not change significantly, as shown in SEM images (Figs. S13(a) and S13(b) in the ESM). Although some areas of the surface are covered with acetylene black, most of the exposed areas can still be seen from the original lamellar frame structure, which was consistent with the initial morphology. The TEM image (Fig. S13(c) in the ESM) provides further details when enlarged. Countless nanosheets are interleaved and overlapping, consistent with the appearance shown in SEM. Further enlarging the edge of FeNiSi (Fig. S13(d) in the ESM) shows that the pore structure in the framework constructed by the nanosheets is well preserved. The structural changes are also characterized by XRD patterns after chronoamperometric test (Fig. S14 in the ESM).

By comparison of LSV curves of OER before and after stability test (Fig. S14(a) in the ESM), it is found that a weak redox peak appeared in the range of 1.2–1.4 V. This phenomenon implies that a small amount of hydroxide may be formed on the surface of FeNiSi during the water splitting process, which is common in various materials [23, 60]. Although no new diffraction peak appeared in the XRD patterns (Fig. S14(b) in the ESM), just the original peak strength is weakened. Considering the morphology and related reports [28, 33], we suspect there is just a small amount of amorphous hydroxide generated on the surface. These results indicate that FeNiSi has excellent structural stability during electrocatalysis. The metal atoms in the silicide structure are separated by silicon atoms in an orderly manner (Fig. 6(e)), which effectively prevents the agglomeration or precipitation of metal

atoms that may occur during the test. So that, the intermetallic silicide can catalyze electrolytic water reaction in a stable and efficient manner. There is another reason why silicide metals may remain highly catalytic, and recent studies have shown that hydrogen evolution and oxygen evolution are mutually promoting processes in alkaline electrolyte, especially under high pressure conditions [13]. The FeNiSi, as a bifunctional electrocatalyst, can continue to provide favorable conditions to promote the reaction as shown in Fig. 6(e).

Considering the result of HER, OER, and overall water splitting, we can draw the conclusion: (i) The defects originated from lattice distortion of FeNiSi can increase the electrocatalytic activity of metal sites; (ii) the large specific surface area can afford plenty of active sites, which can greatly increase the probability of surface reactions; and (iii) abundant pore structure can promote the infiltration of catalyst–electrolyte interface and accelerating the escape of gas bubbles, which is beneficial to the reaction kinetics and stability of a long-term HER/OER operation.

4 Conclusion

In summary, a new synthetic route is developed to prepare intermetallic silicide alloy through a magnesiothermic reduction by using metallic silicate as raw materials. The as-prepared FeNiSi delivers a bifunctional electrocatalytic performance with overpotential of 308 mV for OER and 386 mV for HER at 10 mA·cm⁻² in 1 M KOH. The defects originate from lattice distortion cause a large number of highly active electrocatalytic sites on the surface of FeNiSi. The rich porous structure can further exert the structural advantages caused by lattice distortion, and further increase the number of active sites by expanding the specific surface area. Meanwhile, the porous structure can also improve the stability by improving the reaction kinetics. Consequently, FeNiSi shows a satisfactory durability with an unchanged potential of 1.66 V for overall water splitting at 10 mA·cm⁻² for 15 h. This work not only provides a facile method for the synthesis of intermetallic silicide with considerable porous

structures, but also develops the intermetallic silicide can be considered as the bifunctional electrocatalysts for EWS, which opens up a new avenue for the design and application of intermetallic silicide. The low-cost and efficient intermetallic silicide electrocatalysts can probably provide new opportunities for exploring technologies for renewable energy conversion.

Acknowledgements

This work was supported by the Natural Science Foundation of Liaoning Province (No. 2023-MS-115) and Large Instrument and Equipment Open Foundation of Dalian University of Technology.

Electronic Supplementary Material: Supplementary material (experimental section: materials, material characterizations, and electrochemical characterizations; the XRD patterns and SEM of silicates; mapping images of FeSi and NiSi; XPS full spectra of silicides; FT-IR spectra of $\text{Fe}_x\text{Ni}_{2-x}\text{SiO}_4$ and silicides; CV curves of silicides for HER and OER; EIS spectra for HER and OER; the HER and OER polarization curves of silicides normalized by C_{dl} ; BET specific surface area; and the SEM and TEM images of FeNiSi after chronoamperometric) is available in the online version of this article at <https://doi.org/10.26599/NRE.2023.9120104>.

Declaration of conflicting interests

The authors declare no conflicting interests regarding the content of this article.

Data availability

All data needed to support the conclusions in the paper are presented in the manuscript and/or the Supplementary Materials. Additional data related to this paper may be requested from the corresponding author upon request.

References

- [1] Liu, C.; Li, F.; Ma, L. P.; Cheng, H. M. Advanced materials for energy storage. *Adv. Mater.* **2010**, *22*, E28–E62.
- [2] Schlögl, R. Put the sun in the tank: Future developments in sustainable energy systems. *Angew. Chem., Int. Ed.* **2019**, *58*, 343–348.
- [3] Mu, Y.; Wang, T. T.; Zhang, J.; Meng, C. G.; Zhang, Y. F.; Kou, Z. K. Single-atom catalysts: Advances and challenges in metal-support interactions for enhanced electrocatalysis. *Electrochem. Energy Rev.* **2022**, *5*, 145–186.
- [4] Pei, X. Y.; Mu, Y.; Dong, X. Y.; Ding, C. T.; Xu, L. S.; Cui, M.; Meng, C. G.; Zhang, Y. F. Ion-change promoting Co nanoparticles@N-doped carbon framework on $\text{Co}_2\text{SiO}_4/\text{rGO}$ support forming “double-triple-biscuit” structure boosts oxygen evolution reaction. *Carbon Neutralizat.* **2023**, *2*, 115–126.
- [5] Wang, X.; Gong, J.; Dong, Y.; An, S.; Zhang, X.; Tian, J. Energy band engineering of hydroxyethyl group grafted on the edge of 3D $\text{g-C}_3\text{N}_4$ nanotubes for enhanced photocatalytic H_2 production. *Mater. Today Phys.* **2022**, *27*, 100806.
- [6] Dong, X. Y.; Peng, Y.; Wang, Y.; Wang, H. W.; Jiang, C. M.; Huang, C.; Meng, C. G.; Zhang, Y. F. Hemimorphite /C interface layer with dual-effect methodically redistricted Zn^{2+} deposition behavior for dendrite-free zinc metal anodes. *Energy Storage Mater.* **2023**, *62*, 102937.
- [7] Klemenč, S.; Stegmüller, A.; Yoon, S.; Felser, C.; Tüysüz, H.; Weidenkaff, A. Holistic view on materials development: Water electrolysis as a case study. *Angew. Chem., Int. Ed.* **2021**, *60*, 20094–20100.
- [8] Zhang, H. B.; Zhou, W.; Dong, J. C.; Lu, X. F.; Lou, X. W. Intramolecular electronic coupling in porous iron cobalt (oxy)phosphide nanoboxes enhances the electrocatalytic activity for oxygen evolution. *Energy Environ. Sci.* **2019**, *12*, 3348–3355.
- [9] Sathre, R.; Greenblatt, J. B.; Walczak, K.; Sharp, I. D.; Stevens, J. C.; Ager III, J. W.; Houle, F. A. Opportunities to improve the net energy performance of photoelectrochemical water-splitting technology. *Energy Environ. Sci.* **2016**, *9*, 803–819.
- [10] Wei, Y. M.; Chen, K. Y.; Kang, J. N.; Chen, W. M.; Wang, X. Y.; Zhang, X. Y. Policy and management of carbon peaking and carbon neutrality: A literature review. *Engineering* **2022**, *14*, 52–63.
- [11] Yang, P. J.; Peng, S.; Benani, N.; Dong, L. Y.; Li, X. M.; Liu, R. P.; Mao, G. Z. An integrated evaluation on China’s provincial carbon peak and carbon neutrality. *J. Cleaner Prod.* **2022**, *377*, 134497.
- [12] Wang, Y.; Guo, C. H.; Chen, X. J.; Jia, L. Q.; Guo, X. N.; Chen, R. S.; Zhang, M. S.; Chen, Z. Y.; Wang, H. D. Carbon peak and carbon neutrality in China: Goals, implementation path and prospects. *China Geol.* **2021**, *4*, 720–746.
- [13] Zhang, Z.; Pang, C. X.; Xu, W. C.; Liang, Y. Q.; Jiang, H.; Li, Z. Y.; Wu, S. L.; Zhu, S. L.; Wang, H.; Cui, Z. D. Synthesis and water splitting performance of FeCoNbS bifunctional electrocatalyst. *J. Colloid Interface Sci.* **2023**, *638*, 893–900.
- [14] Mu, Y.; Zhang, Y. F.; Feng, Z. Y.; Dong, X. Y.; Jing, X. Y.; Pei, X. Y.; Zhao, Y. F.; Kou, Z. K.; Meng, C. G. Bifunctional electrocatalyst junction engineering: CoP nanoparticles *in-situ* anchored on $\text{Co}_3(\text{Si}_2\text{O}_5)_2(\text{OH})_2$ nanosheets for highly efficient water splitting. *Chem. Eng. J.* **2023**, *460*, 141709.
- [15] Zeng, Y.; Cao, Z.; Liao, J. Z.; Liang, H. F.; Wei, B. B.; Xu, X.; Xu, H. W.; Zheng, J. X.; Zhu, W. J.; Cavallo, L. et al. Construction of hydroxide pn junction for water splitting electrocatalysis. *Appl. Catal. B: Environ.* **2021**, *292*, 120160.
- [16] Martínez, J.; Mazarío, J.; Olloqui-Sariego, J. L.; Calvente, J. J.; Darawsheh, M. D.; Mínguez-Espallargas, G.; E. Domine, M.; Oña-Burgos, P. Bimetallic intersection in PdFe@FeO_x-C nanomaterial for enhanced water splitting electrocatalysis. *Adv. Sustainable Syst.* **2022**, *6*, 2200096.
- [17] Wang, Z. Q.; Wang, P.; Zhang, H. G.; Tian, W. J.; Xu, Y.; Li, X. N.; Wang, L.; Wang, H. J. Construction of hierarchical IrTe nanotubes with assembled nanosheets for overall water splitting electrocatalysis. *J. Mater. Chem. A* **2021**, *9*, 18576–18581.
- [18] Pu, Z. H.; Liu, T. T.; Zhang, G. X.; Chen, Z. S.; Li, D. S.; Chen, N.; Chen, W. F.; Chen, Z. X.; Sun, S. H. General synthesis of transition-metal-based carbon-group intermetallic catalysts for efficient electrocatalytic hydrogen evolution in wide pH range. *Adv. Energy Mater.* **2022**, *12*, 2200293.
- [19] Wang, J. Y.; He, P. L.; Shen, Y. L.; Dai, L. X.; Li, Z.; Wu, Y.; An, C. H. FeNi nanoparticles on $\text{Mo}_2\text{TiC}_2\text{T}_x$ MXene@nickel foam as robust electrocatalysts for overall water splitting. *Nano Res.* **2021**, *14*, 3474–3481.
- [20] Li, W. J.; Deng, Y. Q.; Luo, L.; Du, Y. S.; Cheng, X. H.; Wu, Q. Nitrogen-doped $\text{Fe}_2\text{O}_3/\text{NiTe}_2$ as an excellent bifunctional electrocatalyst for overall water splitting. *J. Colloid Interface Sci.* **2023**, *639*, 416–423.
- [21] Huang, C. Q.; Zhou, Q. C.; Duan, D. S.; Yu, L.; Zhang, W.; Wang, Z. Z.; Liu, J.; Peng, B. W.; An, P. F.; Zhang, J. et al. The rapid self-reconstruction of Fe-modified Ni hydroxysulfide for efficient and stable large-current-density water/seawater oxidation. *Energy Environ. Sci.* **2022**, *15*, 4647–4658.
- [22] Da, P. F.; Zheng, Y.; Hu, Y.; Wu, Z. L.; Zhao, H. Y.; Wei, Y. C.; Guo, L. C.; Wang, J. J.; Wei, Y. P.; Xi, S. B. et al. Synthesis of bandgap-tunable transition metal sulfides through gas-phase cation exchange-induced topological transformation. *Angew. Chem., Int. Ed.* **2023**, *135*, e202301802.
- [23] Hu, Y.; Zheng, Y.; Jin, J.; Wang, Y. T.; Peng, Y.; Yin, J.; Shen, W.; Hou, Y. C.; Zhu, L.; An, L. et al. Understanding the sulphur-oxygen exchange process of metal sulphides prior to oxygen evolution reaction. *Nat. Commun.* **2023**, *14*, 1949.
- [24] Huang, X. B.; Zheng, H. Y.; Lu, G. L.; Wang, P.; Xing, L. W.;

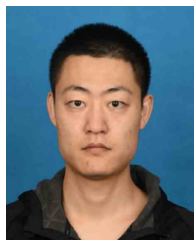
- Wang, J. J.; Wang, G. Enhanced water splitting electrocatalysis over MnCo_2O_4 via introduction of suitable Ce content. *ACS Sustainable Chem. Eng.* **2019**, *7*, 1169–1177.
- [25] Kim, J. S.; Park, I.; Jeong, E. S.; Jin, K.; Seong, W. M.; Yoon, G.; Kim, H.; Kim, B.; Nam, K. T.; Kang, K. Amorphous cobalt phyllosilicate with layered crystalline motifs as water oxidation catalyst. *Adv. Mater.* **2017**, *29*, 1606893.
- [26] Imtiaz, S.; Kapuria, N.; Amiin, I. S.; Sankaran, A.; Singh, S.; Geaney, H.; Kennedy, T.; Ryan, K. M. Directly deposited antimony on a copper silicide nanowire array as a high-performance potassium-ion battery anode with a long cycle life. *Adv. Funct. Mater.* **2023**, *33*, 2209566.
- [27] Qiu, P. F.; Cheng, J.; Chai, J.; Du, X. L.; Xia, X. G.; Ming, C.; Zhu, C. X.; Yang, J.; Sun, Y. Y.; Xu, F. et al. Exceptionally heavy doping boosts the performance of iron silicide for refractory thermoelectrics. *Adv. Energy Mater.* **2022**, *12*, 2200247.
- [28] Mondal, I.; Hausmann, J. N.; Vijaykumar, G.; Mebs, S.; Dau, H.; Driess, M.; Menezes, P. W. Nanostructured intermetallic nickel silicide (Pre)catalyst for anodic oxygen evolution reaction and selective dehydrogenation of primary amines. *Adv. Energy Mater.* **2022**, *12*, 2200269.
- [29] Chen, H.; Zhang, M. C.; Zhang, K. X.; Li, Z. Y.; Liang, X.; Ai, X.; Zou, X. X. Screening and understanding lattice silicon-controlled catalytically active site motifs from a library of transition metal-silicon intermetallics. *Small* **2022**, *18*, 2107371.
- [30] Zhang, B. P.; Gu, Q. F.; Zhang, H. Y.; Yu, X. B. Graphene confined intermetallic magnesium silicide nanocrystals with highly exposed (2 2 0) facets for anisotropic lithium storage. *Chem. Eng. J.* **2021**, *419*, 129660.
- [31] Kumar, R.; Bahri, M.; Song, Y.; Gonell, F.; Thomas, C.; Ersen, O.; Sanchez, C.; Laberty-Robert, C.; Portehault, D. Phase selective synthesis of nickel silicide nanocrystals in molten salts for electrocatalysis of the oxygen evolution reaction. *Nanoscale* **2020**, *12*, 15209–15213.
- [32] Hausmann, J. N.; Beltrán-Suito, R.; Mebs, S.; Hlukhy, V.; Fässler, T. F.; Dau, H.; Driess, M.; Menezes, P. W. Evolving highly active oxidic iron(III) phase from corrosion of intermetallic iron silicide to master efficient electrocatalytic water oxidation and selective oxygenation of 5-hydroxymethylfurfural. *Adv. Mater.* **2021**, *33*, 2008823.
- [33] Chang, W. J.; Sim, E. S.; Kwon, J.; Jang, S.; Jeong, D. Y.; Song, T.; Oh, N.; Jang, H. W.; Chung, Y. C.; Park, W. I. Self-adaptive evolution of nickel silicide nanowires for the enhancement of bifunctional electrocatalytic activities. *Chem. Eng. J.* **2022**, *434*, 134668.
- [34] Jiang, Y. Z.; Li, Z. H.; Li, B. B.; Zhang, J. Y.; Niu, C. M. Ni_3Si_2 nanowires grown *in situ* on Ni foam for high-performance supercapacitors. *J. Power Sources* **2016**, *320*, 13–19.
- [35] Zhang, H.; Zhong, X.; Shaw, J. C.; Liu, L. X.; Huang, Y.; Duan, X. F. Very high energy density silicide-air primary batteries. *Energy Environ. Sci.* **2013**, *6*, 2621–2625.
- [36] Liu, W.; Yin, K.; Zhang, Q. J.; Uher, C.; Tang, X. F. Eco-friendly high-performance silicide thermoelectric materials. *Natl. Sci. Rev.* **2017**, *4*, 611–626.
- [37] Lin, Y. C.; Chen, Y.; Xu, D.; Huang, Y. Growth of nickel silicides in Si and Si/SiO_x core/shell nanowires. *Nano Lett.* **2010**, *10*, 4721–4726.
- [38] Liu, T.; Zhang, H. Y.; Wang, F.; Shi, J.; Ci, P.; Wang, L. W.; Ge, S. L.; Wang, Q. J.; Chu, P. K. Three-dimensional supercapacitors composed of $\text{Ba}_{0.65}\text{Sr}_{0.35}\text{TiO}_3$ (BST)/ NiSi_2 /silicon microchannel plates. *Mater. Sci. Eng. B* **2011**, *176*, 387–392.
- [39] Chen, Y.; Lin, Y. C.; Zhong, X.; Cheng, H. C.; Duan, X. F.; Huang, Y. Kinetic manipulation of silicide phase formation in Si nanowire templates. *Nano Lett.* **2013**, *13*, 3703–3708.
- [40] Song, Y.; Casale, S.; Miche, A.; Montero, D.; Laberty-Robert, C.; Portehault, D. Converting silicon nanoparticles into nickel iron silicide nanocrystals within molten salts for water oxidation electrocatalysis. *J. Mater. Chem. A* **2022**, *10*, 1350–1358.
- [41] Zhang, M. J.; Hu, X. M.; Xin, Y.; Wang, L. K.; Zhou, Z.; Yang, L.; Jiang, J. Z.; Zhang, D. P. FeNi coordination polymer based highly efficient and durable bifunction oxygen electrocatalyst for rechargeable zinc-air battery. *Sep. Purif. Technol.* **2023**, *308*, 122974.
- [42] Zaffran, J.; Stevens, M. B.; Trang, C. D. M.; Nagli, M.; Shehadeh, M.; Boettcher, S. W.; Caspary Toroker, M. Influence of electrolyte cations on Ni(Fe)OOH catalyzed oxygen evolution reaction. *Chem. Mater.* **2017**, *29*, 4761–4767.
- [43] Wang, Q. S.; Zhang, Y. F.; Hu, T.; Meng, C. G. Fe_3O_4 nanoparticles/polymer immobilized on silicate platelets for crude oil recovery. *Microporous Mesoporous Mater.* **2019**, *278*, 185–194.
- [44] Zhao, J.; Zhang, Y. F.; Zhang, S. Q.; Wang, Q. S.; Chen, M.; Hu, T.; Meng, C. G. Synthesis and characterization of Mn-silicalite-1 by the hydrothermal conversion of Mn-magadiite under the neutral condition and its catalytic performance on selective oxidation of styrene. *Microporous Mesoporous Mater.* **2018**, *268*, 16–24.
- [45] Ryu, J.; Hong, D.; Choi, S.; Park, S. Synthesis of ultrathin Si nanosheets from natural clays for lithium-ion battery anodes. *ACS Nano* **2016**, *10*, 2843–2851.
- [46] Liao, Y. Y.; He, R. C.; Pan, W. H.; Li, Y.; Wang, Y. Y.; Li, J.; Li, Y. X. Lattice distortion induced Ce-doped NiFe-LDH for efficient oxygen evolution. *Chem. Eng. J.* **2023**, *464*, 142669.
- [47] Li, M.; Li, H.; Jiang, X. C.; Jiang, M. Q.; Zhan, X.; Fu, G. T.; Lee, J. M.; Tang, Y. W. Gd-induced electronic structure engineering of a NiFe-layered double hydroxide for efficient oxygen evolution. *J. Mater. Chem. A* **2021**, *9*, 2999–3006.
- [48] Lee, S. H.; Kim, J.; Chung, D. Y.; Yoo, J. M.; Lee, H. S.; Kim, M. J.; Mun, B. S.; Kwon, S. G.; Sung, Y. E.; Hyeon, T. Design principle of Fe-N-C electrocatalysts: How to optimize multimodal porous structures. *J. Am. Chem. Soc.* **2019**, *141*, 2035–2045.
- [49] Xuan, C. J.; Wang, J.; Xia, W. W.; Peng, Z. K.; Wu, Z. X.; Lei, W.; Xia, K. D.; Xin, H. L.; Wang, D. L. Porous structured Ni-Fe-P nanocubes derived from a prussian blue analogue as an electrocatalyst for efficient overall water splitting. *ACS Appl. Mater. Interfaces* **2017**, *9*, 26134–26142.
- [50] Lin, G. X.; Ju, Q. J.; Liu, L. J.; Guo, X. Y.; Zhu, Y.; Zhang, Z.; Zhao, C. D.; Wan, Y. J.; Yang, M. H.; Huang, F. Q. et al. Caged-cation-induced lattice distortion in bronze TiO_2 for cohering nanoparticulate hydrogen evolution electrocatalysts. *ACS Nano* **2022**, *16*, 9920–9928.
- [51] Gan, T. J.; Wu, J. P.; Liu, S.; Ou, W. J.; Ling, B.; Kang, X. W. Low-crystallinity and heterostructured AuPt-Ru@CNTs as highly efficient multifunctional electrocatalyst. *J. Electrochem.* **2022**, *28*, 2201241.
- [52] Lefki, K.; Muret, P.; Bustarret, E.; Boutarek, N.; Madar, R.; Chevrier, J.; Derrien, J.; Brunel, M. Infrared and Raman characterization of beta iron silicide. *Solid State Commun.* **1991**, *80*, 791–795.
- [53] Gong, M.; Li, Y. G.; Wang, H. L.; Liang, Y. Y.; Wu, J. Z.; Zhou, J. G.; Wang, J.; Regier, T.; Wei, F.; Dai, H. J. An advanced Ni-Fe layered double hydroxide electrocatalyst for water oxidation. *J. Am. Chem. Soc.* **2013**, *135*, 8452–8455.
- [54] Ma, W.; Ma, R. Z.; Wang, C. X.; Liang, J. B.; Liu, X. H.; Zhou, K. C.; Sasaki, T. A superlattice of alternately stacked Ni-Fe hydroxide nanosheets and graphene for efficient splitting of water. *ACS Nano* **2015**, *9*, 1977–1984.
- [55] Jing, X. Y.; Zhang, Y. F.; Dong, X. Y.; Mu, Y.; Meng, C. G. Manganese silicate nanosheets for quasi-solid-state hybrid supercapacitors. *ACS Appl. Nano Mater.* **2021**, *4*, 8173–8183.
- [56] He, W. J.; Zhang, R.; Cao, D.; Li, Y.; Zhang, J.; Hao, Q. Y.; Liu, H.; Zhao, J. L.; Xin, H. L. Super-hydrophilic microporous $\text{Ni(OH)}_x/\text{Ni}_3\text{S}_2$ heterostructure electrocatalyst for large-current-density hydrogen evolution. *Small* **2023**, *19*, 2205719.
- [57] Zeng, L. Y.; Sun, K. A.; Chen, Y. J.; Liu, Z.; Chen, Y. J.; Pan, Y.; Zhao, R. Y.; Liu, Y. Q.; Liu, C. G. Neutral-pH overall water splitting catalyzed efficiently by a hollow and porous structured ternary

nickel sulfoselenide electrocatalyst. *J. Mater. Chem. A* **2019**, *7*, 16793–16802.

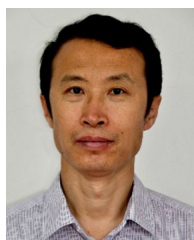
- [58] Mu, Y.; Zhang, Y. F.; Pei, X. Y.; Dong, X. Y.; Kou, Z. K.; Cui, M.; Meng, C. G. Dispersed FeO_x nanoparticles decorated with Co₂SiO₄ hollow spheres for enhanced oxygen evolution reaction. *J. Colloid Interface Sci.* **2022**, *611*, 235–245.
- [59] Cai, Z. X.; Gou, H.; Ito, Y.; Tokunaga, T.; Miyauchi, M.; Abe, H.;

Fujita, T. Nanoporous ultra-high-entropy alloys containing fourteen elements for water splitting electrocatalysis. *Chem. Sci.* **2021**, *12*, 11306–11315.

- [60] Thiyagarajan, D.; Gao, M. Y.; Sun, L.; Dong, X. C.; Zheng, D. H.; Abdul Wahab, M.; Will, G.; Lin, J. J. Nanoarchitected porous Cu-CoP nanoplates as electrocatalysts for efficient oxygen evolution reaction. *Chem. Eng. J.* **2022**, *432*, 134303.



Xuyang Jing is now studying for his Ph.D. degree under the supervision of Prof. Changgong Meng and Associate Prof. Yifu Zhang at the School of Chemical Engineering at Dalian University of Technology (DUT). He received his Master's degree from the Liaoning Normal University in 2018, and received his Bachelor's degree from the Guizhou University. His current research interests are silicate-based supercapacitor and water splitting.



Changgong Meng works in School of Chemical Engineering at Dalian University of Technology (DUT). Now he is the President of Dalian University (2019–present). He has compiled and published 4 textbooks and presided over the construction of 2 national excellent courses. His research field focuses on inorganic functional materials. He has published more than 200 academic papers. He has received many awards, including the Baosteel Education Foundation Outstanding Teacher Award (2001) and the National Outstanding Teacher Award (2006).



Yifu Zhang works in School of Chemical Engineering at Dalian University of Technology (DUT). He received his Bachelor's degree (2008) and Ph.D. degree (2013) from Wuhan University. During 2018.12–2019.12, he worked with Prof. John Wang as a visiting scholar at the Department of Materials Science and Engineering, National University of Singapore. His current research focuses on vanadium oxides, silicates and their carbon composites for energy storage and conversion including supercapacitors, aqueous Zn-ion batteries, and oxygen evolution reaction. He has published more than 200 papers in peer-reviewed journals. He is selected as Elsevier China Highly Cited Scholar (2019) and RSC Highly Cited Top 1% (2019).